3

Photorefractive Materials and Devices for Passive Components in WDM Systems

Claire Gu[a], Yisi Liu[a], Yuan Xu[b], J.J. Pan[b], Fengqing Zhou[b], Liang Dong[b], and Henry He[b]

[a]*Department of Electrical Engineering, University of California, Santa Cruz, CA 95064, USA*
[b]*Lightwaves 2020 Inc., 1323 Great mall Drive, Milpitas, CA 95035, USA*

Abstract

The photorefractive effect is a phenomenon in which the local index of refraction is changed by the spatial variation of the light intensity. Although the phrase "photorefractive effect" has been traditionally used for such effects in electro-optic materials, new materials, including photopolymers and photosensitive glasses, have been developed in recent years and are playing increasingly important roles in optical fiber communication systems. Photopolymers in combination with liquid crystals are ideal materials for wavelength selective tunable devices. The improved optical quality and large dynamic range of photopolymers make them promising materials for holographic recording. Holographic gratings recorded in photopolymers can be employed as distributed Bragg reflectors (DBR). The large birefringence of liquid crystals can be used to tune the index of refraction to cover a large wavelength range (e.g., 40 nm). In addition, the combination of photopolymer and liquid crystal also leads to a new material known as holographic polymer dispersed liquid crystal (H-PDLC) which provides a medium for switchable holograms. Photonic devices made of these materials can be easily incorporated into an optical fiber system because of the low index of refraction of polymers and liquid crystals. Besides photopolymers, photosensitive glasses are also promising for applications in fiber optic systems. Fiber Bragg gratings (FBG) have been used as bandpass filters and dispersion compensators. In this chapter, we describe the applications of photopolymers, H-PDLCs, and FBGs in fiber optic devices. Specifically, some of the recent works on photonic devices such as filters, switches, and high performance dispersion compensators for wavelength division multiplexing (WDM) systems will be described.

3.1. INTRODUCTION

As computers and the Internet become faster and faster, more and more information is transmitted, received, processed, and stored everyday. The demand for high speed and large capacity information systems is pushing scientists and engineers to explore all

possible approaches including electrical and optical means. Optical data storage and fiber communications have already demonstrated their potential in the competition against other technologies. CD and DVD are showing their advantages in the computer and entertainment market. Optical fiber networks are offering unprecedented bandwidth in communications. What motivated the use of optical waves to transmit, process, store and access information is that light or an optical wave has an enormous capacity (or bandwidth) to carry information because of its short wavelength and parallel nature. Photorefractive materials, including traditional electro-optic photorefractive crystals as well as photopolymers and photosensitive glasses, have demonstrated their potential in information systems.

The conventional photorefractive effect [1] is an optical phenomenon in some electro-optic crystals where the local index of refraction is changed by the spatial variation of the light intensity. Such an effect was first discovered in $LiNbO_3$ crystals in the 1960s. The spatial index variation leads to the distortion of the wave front, and such an effect was referred to as "optical damage." The photorefractive effect has since been observed in many other electro-optic crystals, including $BaTiO_3$, $KNbO_3$, SBN, BSO, BGO, GaAs, CdTe, InP, etc. The photorefractive effect is generally believed to arise from optically generated charge carriers which migrate when the crystal is exposed to a spatially varying pattern of illumination with photons having sufficient energy. Migration of the charge carriers due to drift, diffusion and the photovoltaic effect produces a space-charge separation, which then gives rise to a strong space-charge field. Such a field induces a refractive index change via the electro-optic (Pockels) effect. This simple picture of the photorefractive effect can be employed to explain several interesting optical phenomena in these media.

Photorefractive materials are, by far, the most efficient media for the recording of volume dynamic holograms. In these media, information can be stored, retrieved and erased by the illumination of light, in real time. The holographic recording can be employed for 3D optical data storage with an ultra-high density, such a scheme of volume holographic storage offers the unique property of parallel readout with an extremely short access time. In addition to the efficient holographic response, beam coupling known as two-wave mixing (TWM) occurs naturally in photorefractive media. When two beams of coherent radiation intersect inside a photorefractive medium, a stationary index grating is formed. This index grating is spatially shifted by $\pi/2$ relative to the intensity pattern. Such a spatial phase shift leads to nonreciprocal energy transfer when these two beams propagate through the medium. The unique property of nonreciprocal energy transfer can be employed for many applications, including laser beam clean-up, photorefractive resonators, nonreciprocal transmission window, biased elements for laser gyros, self-pumped phase conjugators, mutually pumped phase conjugators, optical interconnection, neural networks, phase conjugate interferometry, etc. It is important to note that the direction of energy flow in TWM is determined by the orientation of the crystal. In addition to holographic storage and TWM, photorefractive crystals are also efficient media for four-wave mixing (FWM) which is a generic process for the generation of phase conjugate waves. Optical FWM with various boundary conditions can be employed to construct several different types of phase conjugators including, externally-pumped phase conjugators, ring conjugators, self-pumped phase conjugators (SPPC), mutually-pumped phase conjugators (MPPC), etc.

Unconventional photorefractive materials including photopolymers and photosensitive glasses are attracting more and more attention for better materials needed in fabrication of fiber optic devices. Traditional photorefractive materials, such as $LiNbO_3$, have been widely used to record holographic gratings in the applications of optical data storage, information processing, and fiber optic devices. However, new materials with larger

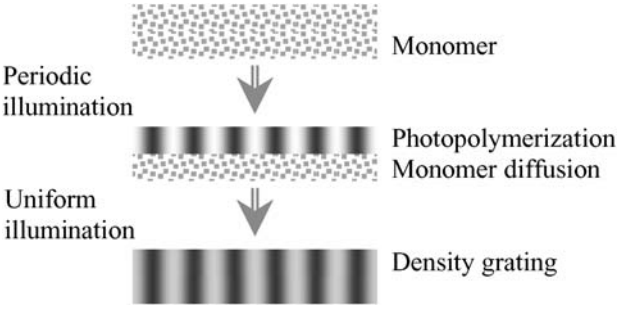

FIGURE 3.1. Grating formation in a photopolymer.

dynamic range, higher photo-sensitivity, lower refractive index, and relatively easier fabrication and integration processes are desirable for these applications, particularly in fiber optic devices.

Photopolymers in combination with liquid crystals are ideal materials for wavelength selective tunable devices. The improved optical quality and large dynamic range of photopolymers make them promising materials for holographic recording. Holographic gratings recorded in photopolymers can be employed as distributed Bragg reflectors (DBR). The large birefringence of liquid crystals can be used to tune the index of refraction to cover a large wavelength range. In addition, the combination of photopolymers and liquid crystals also leads to a new material known as holographic polymer dispersed liquid crystal (H-PDLC), which provides a medium for switchable holograms. Besides photopolymers, photosensitive glasses are also promising for applications in fiber optic systems. Fiber Bragg gratings (FBG) have been used as bandpass filters and dispersion compensators.

New and improved photopolymers have been developed as a result of the search for better holographic materials for optical data storage [2,3]. Figure 3.1 illustrates the process of grating formation in a photopolymer. A photopolymer, before exposed to light, consists of photopolymerizable monomers dispersed in a matrix. Upon illumination by a spatially varying light pattern (sinusoidal intensity pattern generated by two interfering plane waves, for example) monomers in the bright areas become polymers. At the same time, the remaining monomers will diffuse to form a uniform distribution throughout the bulk of the medium. The sum of polymers and monomers form a density gratings, which can be fixed by a uniform illumination after the diffusion of monomers reaches a steady state. As the index of refraction of the polymer depends on its density, the density grating results in an index grating. Since the photopolymerization process is irreversible, gratings recorded in photopolymers are permanent and not optically erasable. The advantages of photopolymers are their relatively large dynamic range and nonvolatile nature. One problem with photopolymers is that the material shrinks during polymerization leading to a Bragg mismatch at read-out. In recent years, there has been significant effort [4–6] to improve the properties of photopolymers, such as higher optical quality, increased thickness, lower shrinkage, as well as larger dynamic range and higher photosensitivity.

A holographic polymer dispersed liquid crystal (H-PDLC) is a photopolymer mixed with liquid crystal (LC). During the grating formation inside the photopolymer–LC mixture, photopolymerization occurs in the bright regions faster than in the dark regions. While the monomer diffuses to the bright regions, the LC molecules diffuse to dark regions [7]. After the final uniform curing, the H-PDLC composite system consists of alternating layers of polymer planes and LC rich droplet planes. If the refractive index of the polymer is

matched with one of the principal refractive indices (n_o or n_e) of the LC but not the other, the grating recorded inside the H-PDLC can be switched on or off by an electrical field that changes the orientation of the LC molecules.

Photosensitivity in glass was first discovered in optical fibers by Ken Hill et al. in 1978 [8], followed by a breakthrough by Gerry Meltz et al. in 1989 reporting on holographic writing of gratings using single-photon absorption at 244 nm [9]. After that, fiber Bragg gratings (FBG) have found numerous applications in fiber optic devices, although the mechanisms of grating formation in photosensitive glass are still under investigation [10,11]. Two of the mechanisms are believed to be involved in the formation of index gratings in germanosilicate fibers: the formation of color centers that changes the index of refraction via Kramers-Kronig relationship and the densification that occurs inside glass fibers upon illumination by UV light.

In this chapter, we describe some recent works on photonic devices such as filters, switches, and dispersion compensators for WDM systems. Photopolymers, H-PDLCs, or photosensitive glass fibers are shown to be the material of choice in the fabrication of these devices.

3.2. TUNABLE FLAT-TOPPED FILTER

As an example, one of the devices that employs photorefractive materials a flat-topped tunable filter [12] for wavelength division multiplexing (WDM) optical networks. A photopolymer can be employed in the implementation of such a filter. As we know, WDM is one of the most promising technologies for increasing the information capacity of optical fiber communication. With WDM, multiple channels at closely spaced wavelengths are sent simultaneously over the same fiber. One of the essential components for WDM is a wavelength selective filter. Previously, several WDM filters have been proposed and discussed. However, these filters do not simultaneously satisfy the two important requirements of a WDM filter: wavelength tunability and flat-topped pass band. In a recent design, a Fabry-Perot etalon with multiple reflection gratings as the distributed Bragg reflectors (DBRs) is used. The DBRs lead to the flat-topped line-shape and an electro-optic material inside the Fabry-Perot etalon gives the tunability of the filter. The filter has a flat-topped pass band with about 1 nm linewidth and its wavelength can be tuned over the 40 nm range provided by Er-doped fiber amplifiers (EDFA).

3.2.1. Principle of Operation

The idea is as follows. For a regular Fabry-Perot etalon, the bandwidth of each transmission peak can be very narrow and only one particular wavelength is transmitted with maximum transmission. At this wavelength the roundtrip phase shift is a multiple integer times 2π, i.e.,

$$\phi_{prop} = 2(2\pi/\lambda_m)nL_C = 2m\pi, \tag{3.1}$$

where ϕ_{prop} indicates the phase shift due to propagation, and L_C is the cavity length. The resonant wavelength λ_m (m is an integer) is determined by the optical thickness nL_C of the cavity, and therefore by n, the refractive index of the medium in the cavity.

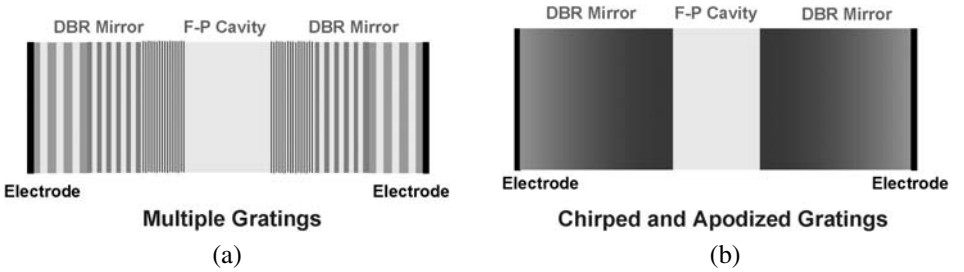

FIGURE 3.2. Fabry-Perot etalon with DBRs. (a) Each DBR consists of multiple spatially separated Bragg gratings. (b) Each DBR consists of a chirped and apodized grating.

Gratings are introduced as DBRs to vary the spectral line shape of the Fabry-Perot etalon. A grating has two functions: (1) a chromatic mirror that reflects light at a wavelength around

$$\lambda_B = 2n\Lambda, \tag{3.2}$$

where Λ is the grating period, n is the refractive index, and λ_B is known as the Bragg wavelength; and (2) a phase shifter that provides additional phase shift to that given in Equation (3.1). The resonant condition for peak transmission with a Fabry-Perot etalon with two symmetric DBRs is now written as

$$\phi_{prop} + 2\phi_{grating} = 2(2\pi/\lambda_m)nL_C + 2\phi_{grating} = 2m\pi, \tag{3.3}$$

where $\phi_{grating}$ is the phase shift upon reflection from each DBR. It is important to note that $\phi_{grating}$ depends on wavelength, as well as grating parameters. In order to have a spectral line-shape with sharp walls (also called tight skirts), one needs a high reflectivity for the DBRs. Therefore, the Fabry-Perot etalon should operate at the wavelength near that given by Equation (3.2). With a single grating DBR, the transmission spectrum still has a peaked line-shape (Lorentzian).

To make the line-shape flat-topped, the Fabry-Perot etalon should resonate at more than one wavelength. This is achieved by using multiple reflection gratings (with different grating period Λ_j, $j = 1, 2, \ldots, N$) as the DBRs. Each of the resonant wavelengths (λ_j, $j = 1, 2, \ldots, N$) results from a pair of gratings with certain grating period (Λ_j, $j = 1, 2, \ldots, N$). With multiple gratings, it is possible to have a narrow range of wavelength approximately satisfying the resonant conditions, Equation (3.3), simultaneously. In this case, the $\phi_{grating}$ in Equation (3.3) is the phase shift upon reflection from all gratings in one end. All wavelengths in this resonant range will have high (near 100%) transmission, resulting in a flat-top. These multiple gratings can be spatially separated, as illustrated in Figure 3.2(a), or they can overlap, or each DBR can be a chirped and apodized grating, as shown in Figure 3.2(b), or a combination of multiple chirped and apodized gratings.

To achieve the tunability, the index of refraction inside the cavity and the background index of refraction of the grating regions need to be modulated (electro-optically, for example).

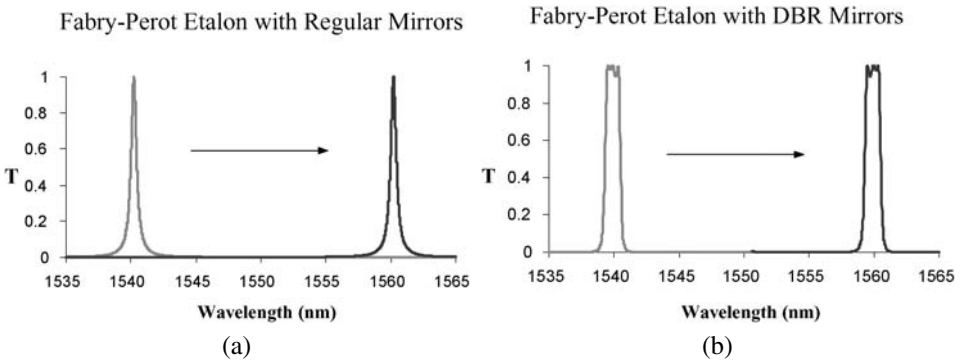

FIGURE 3.3. Comparison between line-shapes of different tunable filters. (a) A regular Fabry-Perot filter. (b) A Fabry-Perot filter with DBRs.

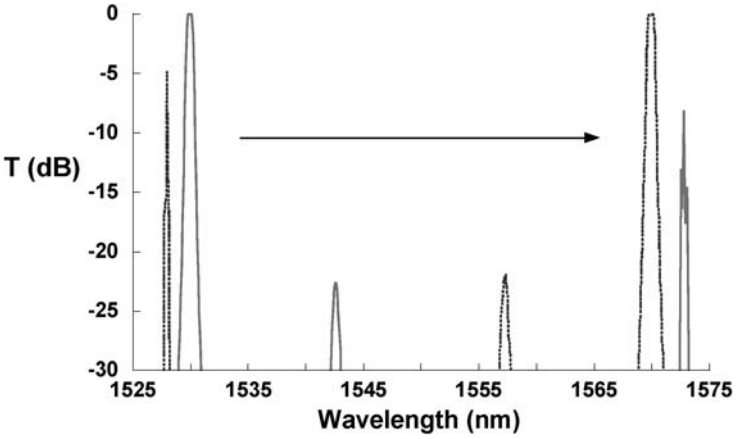

FIGURE 3.4. Transmission spectrum of an optimized flat-topped tunable filter.

3.2.2. Device Simulation

Calculated line-shapes of different tunable filters are compared in Figure 3.3. Figure 3.3(a) shows the transmission spectrum of a Fabry-Perot etalon with regular mirrors. By changing the index of refraction inside the cavity, the transmission peak is tuned from 1540 nm to 1560 nm. Figure 3.3(b) shows the transmission spectrum of a Fabry-Perot etalon with DBRs each consisting of three gratings. The nearly squared line-shape remains throughout the 40 nm tuning range (Figure 3.4) corresponding to the EDFA gain bandwidth. Adjusting grating parameters can minimize the ripples in the high transmission range. In Figure 3.3, we notice that by using DBRs with multiple gratings, the high transmission range is much wider (flat-top) and the slopes of the edges are much steeper (tight skirts). In this design, the pass-band of the filter is well within the stop-band of the DBRs, therefore, the reflectivity of the DBRs is nearly 100%. The tight skirts are achieved by this high reflectivity of the DBRs, therefore high finesse of the Fabry-Perot cavity. A fine tuned DBR with five gratings, two of them chirped, gives us the results shown in Figure 3.4. All side-lobes are either outside the tuning range or below -20 dB. The phase shift upon re-

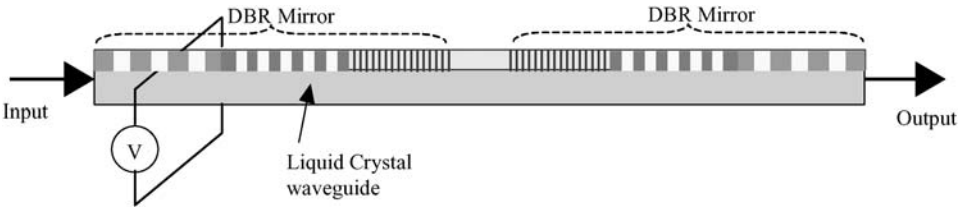

FIGURE 3.5. Schematic of a flat-topped tunable WDM filter based on a liquid crystal waveguide with external gratings, recorded in a layer of photopolymer, as DBRs.

flection from the DBR is calculated using the coupled mode theory. Details of the analysis can be found in Ref. [12].

3.2.3. Design for Implementation

In order to implement the design, one needs to (1) tune the index of refraction both inside the cavity and in the grating region, (2) fabricate the DBRs with multiple gratings. The required large tuning range for the index of refraction ($\Delta n \sim 0.04$) suggests the use of a liquid crystal material. On the other hand, the required interaction length for gratings (100 μm) suggests a holographic medium for the DBRs. The idea to implement a filter that satisfies all the above requirements is shown in Figure 3.5. It consists of a liquid crystal waveguide, whose index of refraction can be tuned by an applied electric field. On top of the liquid crystal waveguide is a layer of holographic material (e.g., photopolymer) which can be used to fabricate the DBRs optically. Multiple exposures in the grating regions can be performed to record multiple holographic gratings. The gratings in the polymer will reflect light waves traveling in the liquid crystal waveguide, therefore serve as DBRs. By applying an electric field across the liquid crystal waveguide, both the index of refraction inside the cavity and the background index of refraction of the grating regions can be tuned simultaneously. The choice of a photopolymer as the holographic material in this case is based on the requirement of low refractive index, permanent gratings, and easy fabrication process.

3.3. WAVELENGTH SELECTIVE 2 × 2 SWITCH

In recent years, the migration of telecom networks to all-optical networks has dramatically increased the demand for all-optical components. DWDM systems capable of increasing the network bandwidth using the currently installed fiber cables have been widely used in the telecommunication systems. Typical DWDM systems require a variety of functional wavelength to be routed throughout the network. Signals need to be optically added and dropped, optically cross-connected and switched. Optical switches with wavelength selectivity are of great importance and application in DWDM systems. One example of such a device is a switchable add/drop module that is capable of switching between all-through state and adding (or dropping) state for the designated wavelength. The building block of this switchable device is an optical add/drop module and a 2 × 2 switch. Most of the existing 2 × 2 switches, such as those involving two prisms operating in total internal reflection mode or total transmission mode, require light being coupled in and out of the fiber resulting in large device size and high insertion loss. Recently, a novel compact-size wavelength-selective switch by recording electrically switchable holographic gratings

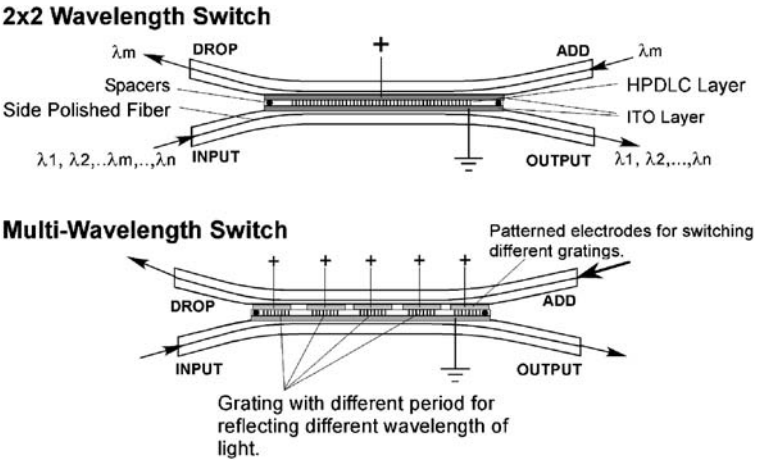

FIGURE 3.6. Structure of the 2×2 wavelength switch and multi-wavelength switch.

in a layer of holographic polymer dispersed liquid crystal (H-PDLC) [13–19] sandwiched between two side-polished fibers was proposed, analyzed and demonstrated. This device provides in-line operation capability and is particularly suitable for WDM network reconfiguration.

A holographic polymer dispersed liquid crystal (H-PDLC) is a photopolymer mixed with liquid crystal (LC). During the grating formation inside the photopolymer-LC mixture, photopolymerization occurs in the bright regions faster than in the dark regions. While the monomer diffuses to the bright regions, the LC molecules diffuse to dark regions [20]. After the final uniform curing (which may be optional if most of the monomer is polymerized during grating recording), the H-PDLC composite system consists of alternating layers of polymer planes and LC rich droplet planes. If the refractive index of the polymer is matched with one of the principal refractive indices (n_o or n_e) of the LC but not the other, the grating recorded inside the H-PDLC can be switched on or off by an electrical field that changes the orientation of the LC molecules.

3.3.1. Principle of Operation

A schematic drawing of the basic structure of the 2×2 wavelength switch is shown in Figure 3.6. Two fibers are partially cut through their claddings by side polishing. The two polished sides are coated with ITO electrodes. Spacers are placed between the two side-polished fibers to form a cell that is then filled with H-PDLC. A holographic grating can be recorded in the H-PDLC layer by interfering two plane waves from a laser. When exposed to an interference pattern, well defined structures of nano-sized LC droplets channels at lower intensity regions interspersed between polymer-chain channels at higher intensity regions will be formed. Due to the different refractive indices of the polymer and the liquid crystal, an index grating is recorded. When an electric field is applied on the H-PDLC layer, the refractive index of the LC can be changed to be the same as that of the polymer. Therefore, the index grating inside the H-PDLC can be switched on or off by the electric field. If one uses two single-mode fibers with slightly different propagation constants, one can avoid directional coupling between the two fibers when the grating is switched off. At the field-on state, the grating is switched off and light will propagate through each

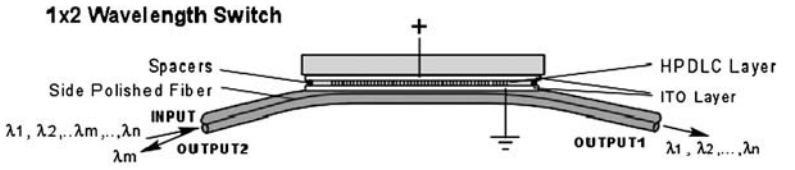

(a) Structure of the 1x2 wavelength switch.

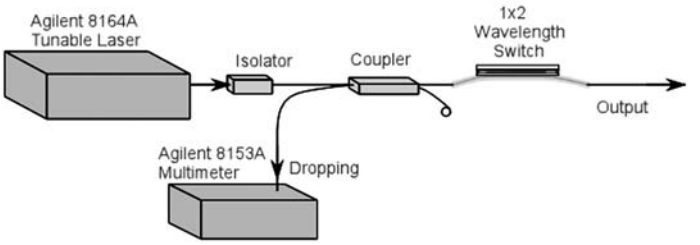

(b) Experimental Setup for measuring the reflection spectrum.

FIGURE 3.7. 1×2 wavelength switch and the experiment setup for demonstrating the device operation.

fiber without any coupling, which provides the all-through state. When there is no electric field, the grating is switched on and the incident light at the INPUT port will be reflected back and come out from the DROP port, which provides the wavelength dropping state. Meanwhile the incident light from the ADD port will be reflected into the OUTPUT port, which provides the wavelength adding state.

3.3.2. Experimental Demonstration

To provide a proof of concept demonstration one side-polished fiber with a H-PDLC cell built on top of it was used. The 1×2 switch structure is shown in Figure 3.7. A Corning SMF-28 fiber was side-polished carefully to a point of 0.5 μm to the core, with a length of 5 mm. ITO coating was deposited onto the polished surface for conduction. Separated by 20 μm spacers an ITO coated glass cover was placed on top of the side polished fiber to form a cell. H-PDLC was introduced into the gap. Then a grating was recorded in the H-PDLC layer by two interfering Ar beams. The angle between the two interfering beams (2θ) was calculated according to $\sin\theta = \bar{n}\lambda_{\mathrm{Ar}}/\lambda$, where λ_{Ar} is the wavelength of the Ar laser (488 nm), λ is the wavelength to be reflected and $\bar{n}$ is the mode index of the corresponding wavelength. To measure the reflected wave, a coupler as shown in Figure 3.7 is placed at the input side.

In the experiment, an Agilent 8164A tunable laser was used as the optical source, an Agilent 8153A multimeter was used to measure the reflected power. A 3 dB coupler was used to split the reflected beam and send half of it to the multimeter; an isolator was used to prevent the other reflected beam from going back into the source. A HP3245A was used to generate a square wave AC signal to drive the switch. The fiber that used in this experiment is a Corning SMF-28 fiber. The parameters are listed in Table 3.1.

TABLE 3.1.
Parameters for 1×2 switch.

Core radius ρ	4.5 μm
Cladding radius	62.5 μm
Core refractive index: n_{core}	1.4505
Cladding refractive index: $n_{cladding}$	1.4447
Distance between the polishing surface to center of the core	5 μm
Grating length	3 mm
Refractive index of H-PDLC	1.502
Thickness of H-DPLC layer	20 μm
Δn of LC in H-PDLC	0.07

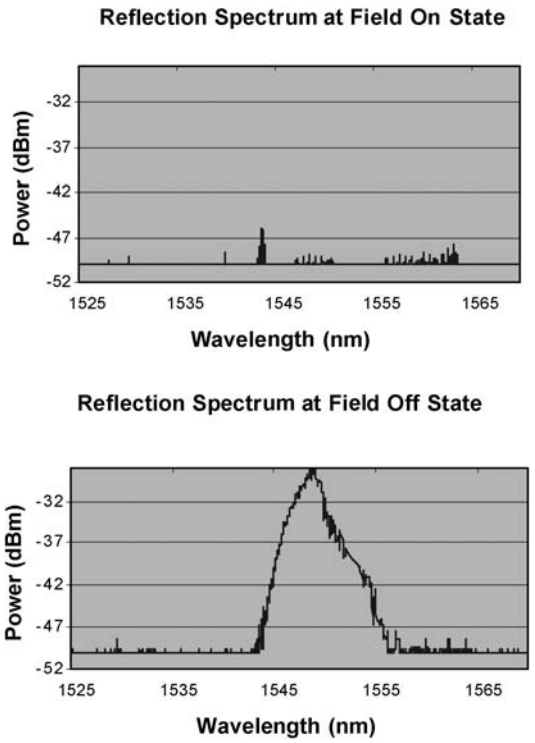

FIGURE 3.8. Reflection spectrum measured at field-on and field-off states of the switch.

The preliminary results of the experiment are shown in Figure 3.8. By adjusting the angle between the two writing beams during the holographic recording a reflection peak at 1548 nm in the field-off state is obtained. The 3 dB bandwidth of the reflection peak is about 3 nm. Adjusting the angle between the two writing beams can control the peak-wavelength of the reflection. When the electric field was applied, the holographic grating was switched off and an extinction ratio of more than 25 dB has been achieved. Further optimization of the experimental condition is expected to improve the results significantly in terms of diffraction efficiency and bandwidth. In this experiment, the H-PDLC has a higher index of refraction than that of the fiber core. In the field-on state, the insertion loss of the device is measured to be 20 dB. This gives us an estimate of the diffraction efficiency of the grating

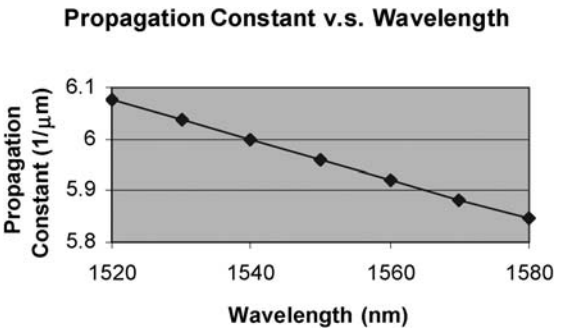

FIGURE 3.9. Propagation Constants calculated for various wavelength in the working range.

to be about 63% (−2 dB). However, the coupling loss due to the high refractive index of the H-PDLC layer can be more than 30 dB. In other words, most of the energy is coupled into the H-PDLC layer and is lost. It is believed that by using an H-PDLC layer with a reduced refractive index, one will be able to minimize the insertion loss. After it is polished to about 5 μm above the core, by using a special polishing technique, the insertion loss is often less than 0.2 dB. By applying low refractive index material on it, it should be able to compensate for the loss at the polished spot. In addition, by adjusting the grating parameters, such as grating length and apodization, etc., one can modify the reflection spectrum to achieve the required bandwidth and line shape. The side-polished fibers can have a polishing length of 10 mm or more.

Simply by replacing the coupler with a circulator and adding another circulator at the output end as the ADD port, one can achieve a Switchable Optical Add/Drop Multiplexer (SOADM). In the field off state, the selected wavelength from the incident light at the input port will be dropped, while the incident light at the ADD port will be added. In the field on state, the grating is invisible due to the matched refractive indices, no light will be added or dropped. By cascading several of these devices, one can also achieve an $N \times N$ Switchable MUX/DEMUX.

Alternatively, all of these devices can also be built based on the 2×2 switch shown in Figure 3.6, where two side-polished fibers are used. In this case, the circulators will no longer be necessary, which provides a more compact and less expensive design.

3.3.3. Theoretical Analysis

To understand the device performance and design improved switches, one needs to analyze the field distribution of the mode in the structure and the coupling between the forward and backward propagating waves. In a recent analysis, they are calculated using the vector modal method [21–26] and the coupled mode theory, respectively.

The modal properties of the D-shaped fiber covered with a dielectric film can be analyzed using the so-called vector modal method, where the field in each region is decomposed into the known eigen-modes of the fiber or slab waveguide, respectively. By matching the boundary conditions the propagation constant and the field distribution can be found. Figure 3.9 shows the propagation constant as a function of the wavelength. As can be noticed, the propagation constant varies almost linearly in the working wavelength range.

Figure 3.10 shows the field distribution inside the complex structure consisting of the D-shaped fiber, the H-PDLC slab waveguide and the outer cladding layer. Since the

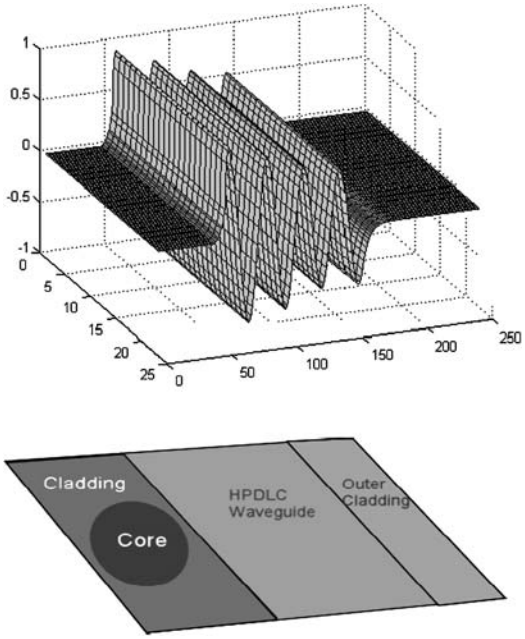

FIGURE 3.10. Field distribution within a side-polished fiber and a (high refractive index) planar waveguide system.

refractive index of the H-PDLC is higher than that of the fiber core, most of the energy is propagating inside the H-PDLC layer. The field remaining inside the fiber core is almost invisible in Figure 3.10. This result explains the high insertion loss that was measured in the experiment.

The coupling between the forward and backward propagating modes is analyzed using the well known coupled mode theory. In the coupled mode equations, the coupling coefficient is given by

$$\kappa = \frac{i\varpi\varepsilon_0 a_l \int_{-\infty}^{\infty}\int_{-\infty}^{\infty} \Delta n^2(x)|E(x,y)|^2 dxdy}{4\int_{-\infty}^{\infty}\int_{-\infty}^{\infty}|E(x,y)|^2 dxdy}, \tag{3.4}$$

where $\Delta n(x)$ is the refractive index variation introduced by the grating and $E(x, y)$ is the modal field distribution. Once the coupling coefficient is found, the peak diffraction efficiency of the grating can be easily obtained by $\eta = \tanh^2(\kappa L)$ where L is the length of the grating. The reflection spectrum of the grating can also be obtained using the coupled mode analysis. Using parameters in the experiment, the reflected power is shown in Figure 3.11. The loss (scattering and absorption) of H-PDLC was experimentally measured to be 0.5 dB/cm, thus the absorption and scattering loss in the system was 0.25 dB (waveguide length was 0.5 cm). From the field distribution, the coupling loss would contribute -25 dB to the total power (including the 3 dB coupler in the system).

Furthermore, Equation (3.4) indicates that a stronger coupling (greater coupling coefficient) calls for a field distribution with a greater percentage of power inside the H-PDLC layer where $\Delta n(x)$ is non-zero. However, as discussed above, a large portion of the energy inside the H-PDLC causes a great insertion loss. The trade-off between the coupling effi-

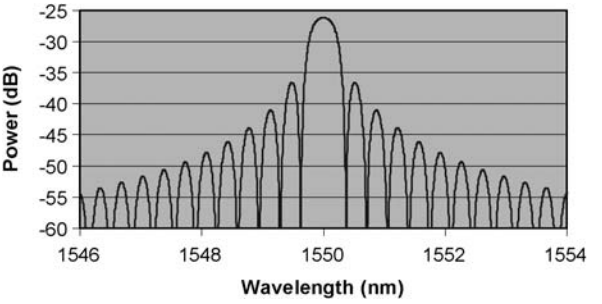

FIGURE 3.11. Theoretical simulation of the spectrum of the 1×2 switch.

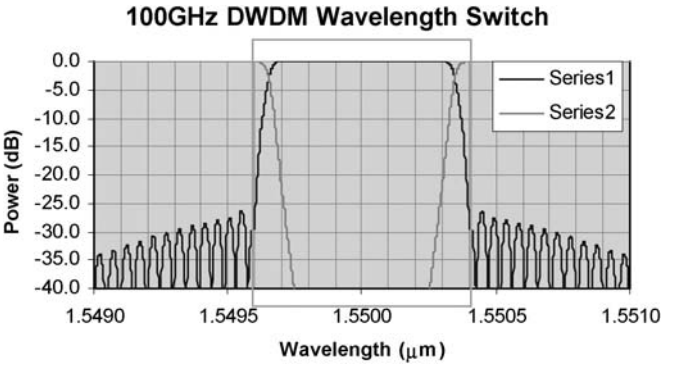

FIGURE 3.12. Spectrum of the 100 GHz DWDM wavelength switch design.

ciency and the insertion loss needs to be taken into consideration when parameters in the design are selected.

3.3.4. Optimized Switch Design

In order for the switch to be practically useful in DWDM systems, it is necessary to improve the performance dramatically. Specifically, it is necessary to decrease the insertion loss, increase the diffraction efficiency to almost 100%, decrease the bandwidth to 100 GHz or 50 GHz, make the line shape flat-topped [27], suppress the side lobes, and increase the switching speed. From the theoretical analysis, the insertion loss can be decreased by reducing the refractive index of the H-PDLC, the diffraction efficiency can be increased by increasing the grating length, the bandwidth and line shape can be modified by the coupling coefficient and the apodization. On the other hand, the trade-off between the coupling coefficient and the insertion loss implies that the refractive index of the H-PDLC cannot be too small. Taking all the restrictions into consideration, the following switches for 100 GHz and 50 GHz DWDM systems, respectively, have been designed.

3.3.4.1. 100 GHz DWDM Wavelength Switch For the 100 GHz DWDM wavelength switch design, the parameters are listed in the following Table 3.2.

Using the transfer matrix method, one can simulate the output spectrum of this device. The result is shown in Figure 3.12. The side-lobes have been successfully suppressed to be less than -26 dB while keeping the bandwidth to be within 0.8 nm. The peak inser-

TABLE 3.2.
Parameters used in 100 GHz DWDM wavelength switch design.

Fiber type	Corning SMF-28
n_{core}	1.4505
$n_{cladding}$	1.4447
r_{core}	9 μm
$r_{cladding}$	125 μm
Distance from the polished surface to core	0.5 μm
Cell thickness	20 μm
$n_{polymer}$	1.4475
Liquid crystal: n_{o}	1.4475
Liquid crystal: n_{e}	1.5125
Δn	0.065
Scattering and absorption loss	0.01 dB/mm
Grating length	16 mm
Apodization envelope function	sinc

TABLE 3.3.
Expected performance of the 100 GHz DWDM wavelength switch.

Switching bandwidth		100 GHz
Channel center wavelength		1550 nm
Reflection band @ 0.2 dB		0.65 nm
Reflection band @ 25 dB		0.8 nm
Channel isolation		>25 dB
Peak insertion loss within reflected band		<0.16 dB
Switching speed:	Rise time:	460 μs
	Fall time:	180 μs
Switching voltage		<200 V

tion loss in the reflection band is only −0.16 dB, which makes this device very desirable for telecommunication.

The switching speed of the H-PDLC cell has been experimentally measured to be a few hundred microseconds. the detailed specification of this design is listed in the following Table 3.3.

3.3.4.2. 50 GHz DWDM Wavelength Switch For the 50 GHz DWDM wavelength switch design, again, a "sinc" apodization envelope function was used to improve the reflection spectrum. The optimized parameters are listed in the following Table 3.4.

The spectrum of this 50 GHz DWDM wavelength switch has been simulated and optimized using the transfer matrix method. The result is shown in Figure 3.13. Notice that the first and the second pair of side-lobes have been suppressed down to less than −32 dB, while the peak insertion loss at the reflection band is only −0.18 dB.

The detailed specification of this 50 GHz DWDM wavelength switch design is listed in Table 3.5.

The switching voltage and switching speed can be further improved. By adjusting the proportion of the ingredients, it is believed that the switching voltage can be lowered to 100 V. By making the curing of H-PDLC more homogeneous, it is also possible to decrease the rise time to less than 200 μs.

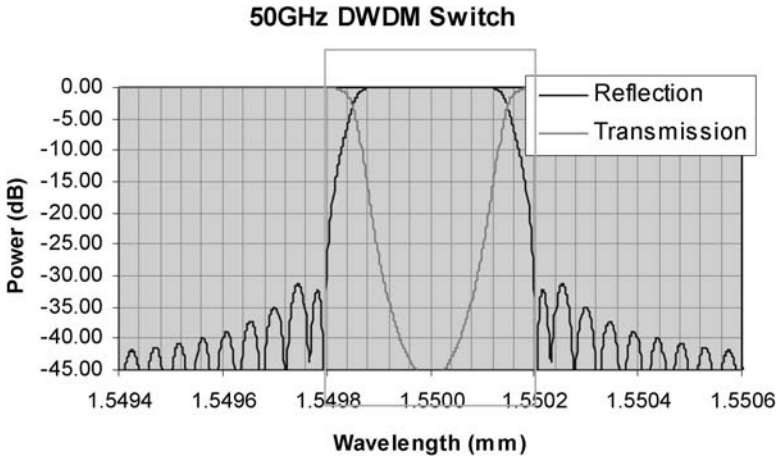

FIGURE 3.13. Spectrum of the 50 GHz DWDM wavelength switch design.

TABLE 3.4.
Optimized parameters used for 50 GHz DWDM wavelength switch design.

Fiber type	Corning SMF-28
n_{core}	1.4505
$n_{cladding}$	1.4447
r_{core}	9 μm
$r_{cladding}$	125 μm
Distance from the polished surface to core	0.5 μm
Cell thickness	20 μm
$n_{polymer}$	1.4475
Liquid crystal: n_o	1.4475
Liquid crystal: n_e	1.4755
Δn	0.028
Scattering and absorption loss	0.01 dB/mm
Grating length	18 mm
Apodization envelope function	sinc

TABLE 3.5.
Expected performance of the designed 50 GHz DWDM wavelength switch.

Switching bandwidth		50 GHz
Channel center wavelength		1550 nm
Reflection band @ 0.2 dB		0.28 nm
Reflection band @ 25 dB		0.4 nm
Channel isolation		>25 dB
Peak insertion loss within reflected band		<0.18 dB
Switching speed:	Rise time	460 μs
	Fall time:	180 μs
Switching voltage		<200 V

3.3.5. Discussion

In this section, a novel in-line 2 × 2 wavelength switch based on H-PDLC gratings sandwiched between two side-polished fibers [28–31] has been discussed. The idea has

been demonstrated experimentally and analyzed theoretically. Based on the experimental and theoretical results, optimized switches for both 100 GHz and 50 GHz DWDM systems have been designed. This device provides the in-line operation capability and is particularly suitable for DWDM network reconfiguration.

In addition, as shown in Figure 3.6, it is possible to build a multi-grating wavelength switch based on the same basic structure. With the polishing technique, the side polished part can be long enough to write several gratings at different spatial locations inside the H-PDLC layer. Using photolithography, patterned electrodes can be fabricated on the ITO layer on one of the side polished fibers. By applying control voltages to each of these electrodes, one will be able to switch the gratings on and off individually, thus choosing different wavelength to be reflected. This structure can be used in wavelength routing.

3.4. HIGH PERFORMANCE DISPERSION COMPENSATORS

Fiber Bragg gratings (FBGs) have been widely used for filters and dispersion compensators. Recently, several high performance dispersion compensators have been designed and implemented. Here, as examples, we present two types of high performance dispersion compensators. One type is a multi-channel dispersion-slope compensator implemented by post writing exposures. The other type is high reflectivity dispersion management filters implemented with a high precision FBG writing set-up.

3.4.1. Multi-Channel Dispersion-Slope Compensator

As transmission speed increases from 2.5 to 10 Gbits/sec and higher, and channel spacing decreases from 200 GHz to 50 GHz, chromatic dispersion and dispersion slope become limiting factors in wavelength division multiplexing (WDM) systems. Several techniques have been proposed for dispersion and dispersion-slope compensation, including: (i) compensation fiber [32,33], which is the most extensively used technology but is expensive and introduces a large amount of loss; (ii) virtual image phased array [34], which has a stability problem; (iii) conventional chirped fiber grating, which is ideal for dispersion compensation and may be used for slope compensation with nonlinear chirp but requires a long grating length to cover enough channels and precise period control to achieve the desired compensation.

Recently, however, sampled fiber Bragg grating (FBG) has attracted attention because of its unique properties, such as multiple reflection/transmission peaks with very precise spacing and relatively easy fabrication procedures compared with long chirped grating writing. These properties make FBG ideal for WDM applications. Multi-channel dispersion compensation has been shown experimentally using sampled chirped FBGs [35], and dispersion slope compensation has been proposed and demonstrated by several sampled grating based techniques. These include the use of a sampled non-linearly-chirped FBG grating [36] and a sampled chirped-grating with a linearly chirped sampling period [37–39]. The sampled nonlinearly chirped grating can also be used for tunable dispersion compensation but it requires precise period control and its channel bandwidth is limited. Theoretically, the chirped sampling period technique [Figure 3.14(a)] holds a lot of promise [37]. For fabrication, however, it requires very precise sampling period control during the grating writing and the grating performance cannot be further modified after writing, which limits repeatability and flexibility.

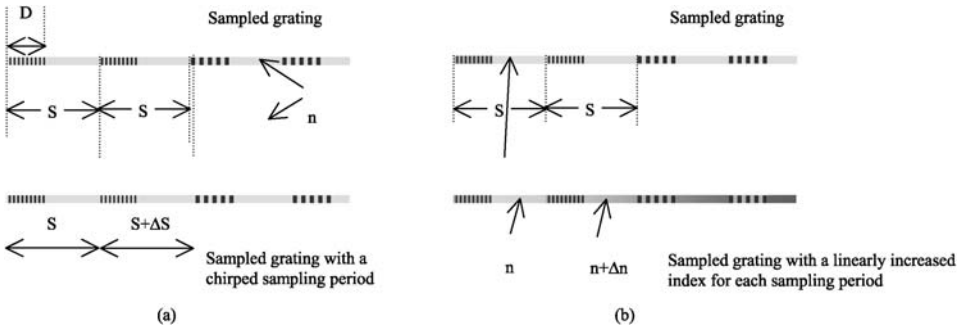

FIGURE 3.14. (a) A sampled grating with a chirped sampling period. (b) A sampled grating with a linearly increased index for each sampling period.

A novel optical fabrication method is used to achieve dispersion-slope compensation based on a sampled linearly chirped FBG with non-uniform refractive index for each sampling period. This grating is relatively easy to be controlled and fabricated and is flexible for different designs. It is demonstrated experimentally in a multi-channel 50 GHz WDM system. The dispersion slope is demonstrated to match that of the Corning LS fiber.

Defining S as sampling period and D as grating length within each sampling period, the optical path length of each non-grating part can be presented by $n(S - D)$, where "n" is the refractive index. Comparing the method of changing the sampling period (Figure 3.14(a), period changing expressed as ΔS) and that of changing the refractive index (represented by Δn) of each sampling period (Figure 3.14(b)) in a sampled grating, they are similar to each other. They both affect the optical path length. Based on this concept, fabricating a sampled grating with a linearly chirped sampling period is equivalent to fabricating a sampled grating with a linearly increased index for each sampling period, as long as $n\Delta S = \Delta n(S - D)$ or $\Delta n/n = \Delta S/(S - D)$. However, adjusting the refractive index is less problematic since Δn can be controlled by applying a UV exposure easily. With a CW laser and step motor control system, a different refractive index in each sampling period can be achieved by post-exposure of UV light with different exposure times. Therefore, a linear or non-linear sampling index profile can be achieved, assuming that the index modulation Δn is proportional to the exposure time Δt. Figure 3.15 shows the procedure for fabricating a sampled chirped grating with a linearly increased index per sampling period. This is equivalent to a sampled chirped grating with a linearly chirped sampling period, which was proposed for dispersion slope compensation [37].

Both simulations and experiments have been done to demonstrate that a sampled chirped grating with a linearly increased refractive index per sampling period is suitable for dispersion slope compensation in a 50 GHz WDM system. A rectangular sampling function and linearly increased index profile were applied, as shown in Figure 3.15.

Figure 3.16 shows the simulation results of a sampled chirped grating's spectrum, group delay (GD) and channel dispersion with a uniform refractive index per sampling period and those with a linearly increased index. It shows that the grating's dispersion has been modified by applying a linearly increased refractive index for each sampling period. The grating's relative dispersion slope (RDS) is optimized to $-0.044\ \text{nm}^{-1}$, which is designed to compensate Corning LS fiber's dispersion slope with RDS equaling to $-0.044\ \text{nm}^{-1}$ [37] (RDS is defined as dispersion slope normalized to dispersion). The grating's sampling period is 2.07 mm, which corresponds to 50 GHz channel spacing, with

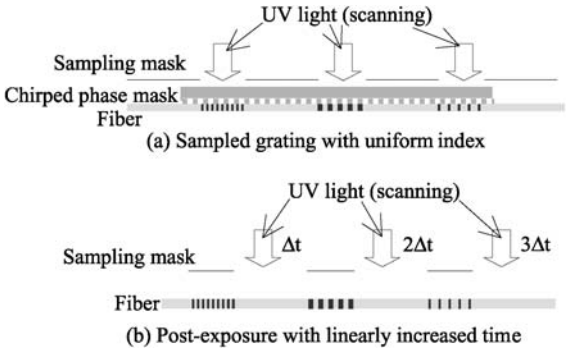

FIGURE 3.15. Schematics of the writing procedure.

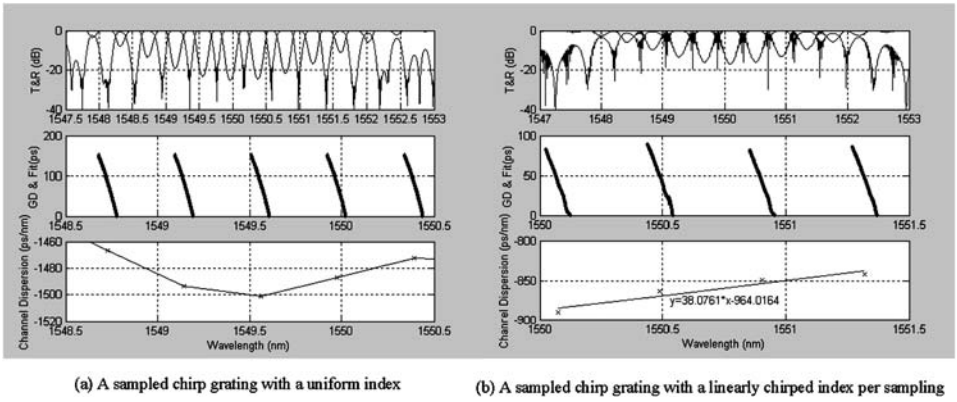

FIGURE 3.16. Simulation results for dispersion slope compensation of a 50 GHz WDM system.

15% duty cycle, defined as D/S. Figure 3.17 shows the experimental results of a sampled chirped grating's spectrum and its channels' dispersion, group delay and group delay ripple (a) before the linear post-exposure and (b) after the linear post-exposure.

In the experiment, the grating was written by a 50 mW 244 nm (frequency doubled Argon) CW laser and a holographic chirped phase mask with a 15% duty cycle sampling mask with 2.07 mm sampling period, which corresponds to 50 GHz channel spacing. The grating's reflection spectrum and group delay were measured by Agilent's "Chromatic Dispersion Test Solution" using a 2 GHz modulation frequency and 10 pm wavelength resolution. The grating length was 60 mm and the fiber was photosensitive and hydrogen loaded. Gaussian apodization was applied to minimize the group delay ripple (GDR).

Before post-exposure, the channel dispersion data points are distributed along a nonlinear curve, while after the post-exposure, these points are lined up along a straight line. With an optimized linearly step-increased index per sampling period, the channels' dispersion slope is adjusted to 23.625 ps/nm^2 and its RDS to -0.042 nm^{-1}, which matches Corning LS fiber's RDS. The relative error of each channel's dispersion compared to the linear fit for the 7 channels is: 0.33%, -0.46%, -0.08%, 0.21%, 1.69%, 5.57%, 1.21%, respectively, which shows that they match very well.

The spectrum's ripple increases with the non-uniform index. This is due to the phase mismatch for each sampling period caused by the linearly increased refractive index. The

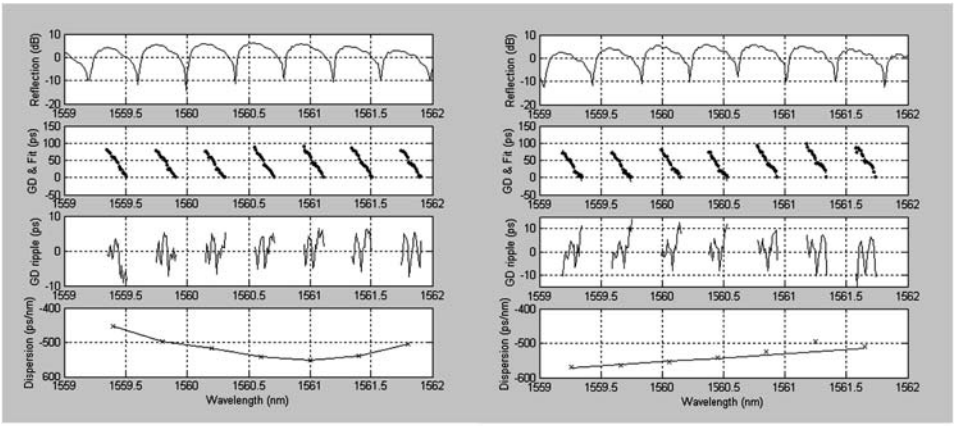

FIGURE 3.17. Experimental results for dispersion slope compensation in a 50 GHz WDM system.

group delay ripple (GDR) also increases, but only slightly. The maximum GDR in (a) is $\sim \pm 8$ ps and is $< \pm 15$ ps in (b) with bandwidth $\sim$0.16 nm for each channel. The channel spacing is 50 GHz (0.4 nm) in both cases with $<$0.5% error while the center wavelength shifts a little after post-exposure.

Photo-sensitivity of the glass plays an essential role in fabricating this device. The potential of using post recording exposure as a method to compensate for dispersion slope is exceptional due to its ease of fabrication, low cost, flexibility and compatibility with other mature fiber grating techniques.

3.4.2. High Precision FBG Fabrication Method and Dispersion Management Filters

The novel writing system used in the experiment is based on a continuous phase-controlled writing configuration similar to those in previous work [40–44]. It allows apodization and phase of the fiber Bragg grating to be continuously controlled at each grating line. Special attentions have been given to interferometer design, minimum timing jitters, precise translation and accurate phase/apodization control. The fiber is moving constantly on a high precision motor with 0.3 nm resolution. A high-speed shutter system with less than 10 ns response time is utilized to repeatedly write small grating structure ($<$200 μm) in the fiber as the fiber moves through the interference pattern. The motion is carefully synchronized with the shutter. A compact ultra stable interferometer design is designed and demonstrated. A phase mask is used to split the writing beam equally at desired angle. To minimize the phase perturbation introduced by any perturbations in the optical path, an out-of-plane bi-directional ring structure based interferometer is used. The interferometer looks similar to a folded Mach-Zehnder with the interfering spot folded back to almost the splitting spot. However, a closer look at the beam paths shows that it is different from a simple folded Mach-Zehnder. Each beam is reflected by one mirror in the interferometer to the other mirror, then to the interfering spot where the fiber is located. After reflected by the mirrors, the two beams return to almost the same spot as the incident beam. With this design, the clockwise and count-clockwise beams travel through almost the same optical path. The phase-delay caused by any variation along the optical path will be experienced by both interference beams. Therefore, on the fiber where the grating is written, the

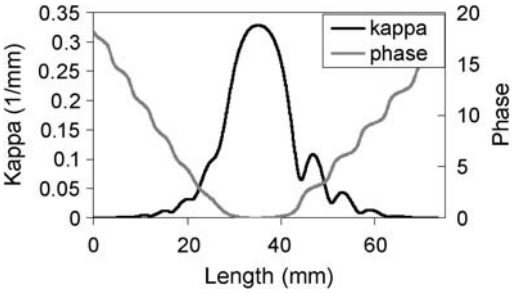

FIGURE 3.18. Grating design for a 25 GHz 99.9% filter with −700 ps/nm of dispersion.

interference pattern's phase remains stable. The fiber grating's phase is varied by the PZT controlled-phase mask, where the phase of interference fringe is accurately adjusted by a closed loop control of the PZT motion.

The first design is a 25 GHz 99.9% grating with a constant −700 ps/nm dispersion, which combines the characters of both dispersion compensator and optical filter. Therefore, the number of components in an optical network is minimized and the network is expected to have a better performance with lower cost. The design is shown in Figure 3.18. The phase structure in gray curve in Figure 3.18 is continuous with smoothed π phase jumps, which is very different from a zero dispersion grating. The coupling coefficient, kappa, does not have the zero-crossings as in a zero dispersion grating associated with the discrete π phase jumps (see the black curve in Figure 3.18). It has some small ripples at the front end and some more pronounced ripples at the back end of the grating. The grating is about 73 mm long. The target reflection and group delay from the design are shown in Figure 3.19 in gray and black solid lines respectively. The measured reflection and group delay are given in gray and black dotted lines respectively. The measured group delay ripple is less than ± 1 ps. It can be seen that a good agreement and performance is achieved for this filter. The target transmission and transmission dispersion are given in black and gray solid lines respectively in Figure 3.20. The measured transmission and transmission dispersion are given in black and gray dotted lines respectively in Figure 3.20. The measured grating has a reflectivity of 99.84%, corresponding to a transmission isolation of 28 dB.

The second design example is a 25 GHz 99.9% grating with a dispersion varying linearly from 1000 ps/nm to −1000 ps/nm. This design is shown in Figure 3.21. Slighted smoothed π phase jumps can be seen in the phase structure along with a slow varying background (see the gray curve in Figure 3.21). The coupling coefficient in black curve in Figure 3.21 bears many similarities to the zero dispersion grating design with many zero-crossings corresponding to the π phase jumps. There is a small asymmetry in the ripples at the two sides of the main peak as well as in the main peak itself. The grating is 72 mm long. This grating has a quadratic delay (see the solid gray line in Figure 3.22). This is very difficult to do by conventional chirp control. But it is, however, easy to do with phase control. The measured delay from a fabricated grating is also shown in Figure 3.22 in gray dotted line. It is in good agreement with the design. The target transmission and transmission dispersion is shown in black and gray solid lines in Figure 3.23, respectively. The measured transmission and transmission dispersion are given in black and gray dotted lines, respectively, in Figure 3.23. The measured grating has a reflectivity of 99.94%, corresponding to a transmission isolation of 32 dB.

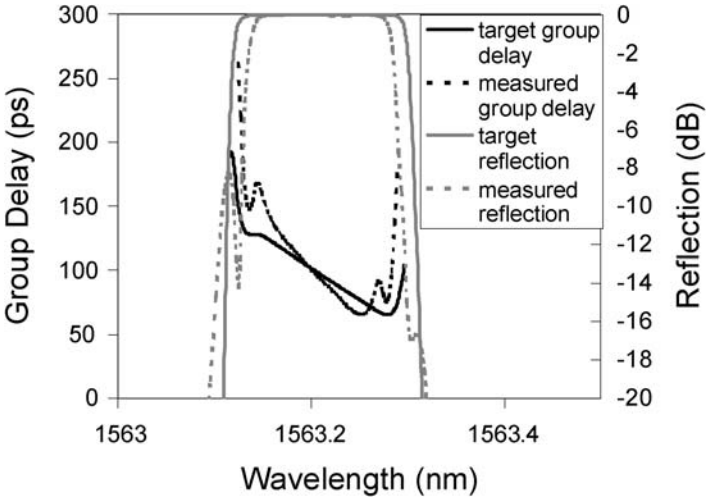

FIGURE 3.19. Target and measured reflection and delay of the grating design shown in Figure 3.18.

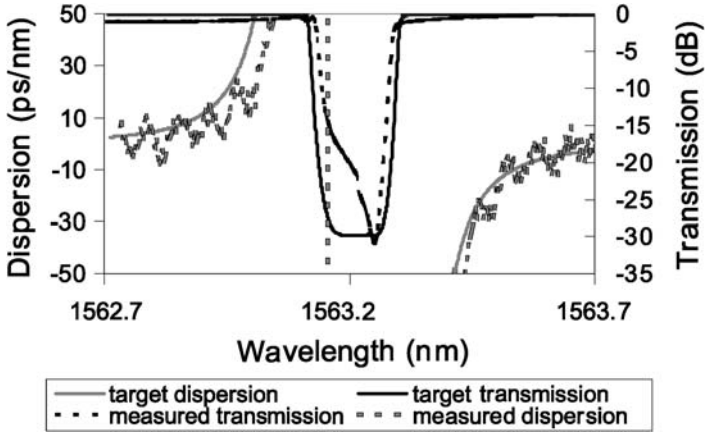

FIGURE 3.20. Target and measured transmission and transmission dispersion of the grating design shown in Figure 3.18.

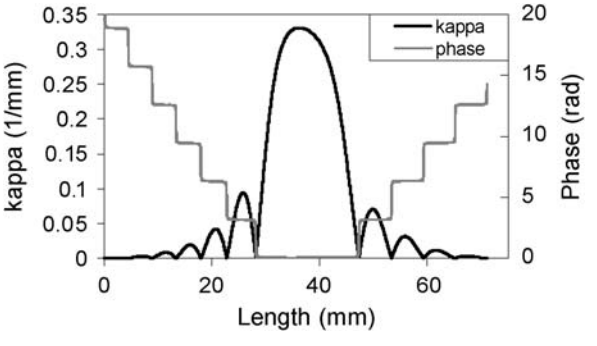

FIGURE 3.21. Grating design for a 25 GHz 99.9% filter with dispersion linearly varying from −1000 ps/nm to 1000 ps/nm.

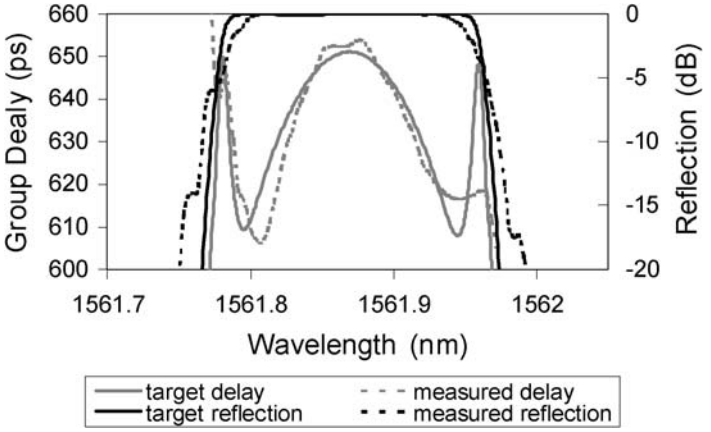

FIGURE 3.22. Target and measured reflection and delay of the grating design shown in Figure 3.21.

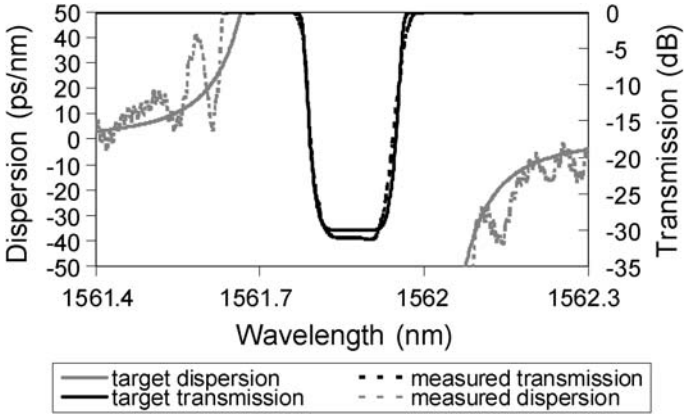

FIGURE 3.23. Target and measured transmission and transmission dispersion with the grating design shown in Figure 3.21.

The two examples here show that optical filters with arbitrarily engineered amplitude and phase and strong enough for sufficient transmission isolation can be accurately achieved by fiber Bragg gratings. This will open up a range of new applications, which have not been possible today.

The ability to continuously control both apodization and phase of a fiber Bragg grating can lead to a large number of new optical filters. The wavelength-division-multiplexing filters with arbitrary amount of chirp can be used at add/drop nodes or terminal nodes to combine the functionalities of filtering and dispersion compensation. This leads to much freedom in designing system dispersion map and location of add/drop nodes. Optical filters with any desired amplitude and phase can be made for various pulses shaping to generate a desired pulse shape and phase from a known in-coming pulse [43]. These filters also enable more freedom in code designs in optical code division multiplexing [44].

3.5. CONCLUSIONS

We have described the applications of photopolymers, H-PDLCs, and FBGs in fiber optic devices. Specifically, as examples, we described a flat-topped tunable WDM filter incorporating DBRs recorded holographically in photopolymers, a wavelength selective switch based on switchable gratings in holographic polymer dispersed liquid crystals, several high performance dispersion compensators using FBGs including a multi-channel dispersion slope compensator using a novel sampled fiber Bragg grating with post recording exposures, and two high reflectivity dispersion management filters. These devices are particularly suitable for WDM networks and have demonstrated the potential for unconventional photorefractive materials to be used in fiber optic devices for WDM systems.

REFERENCES

1. See, for example, P. Yeh and C. Gu, Eds., Landmark Papers on Photorefractive Nonlinear Optics, World Scientific, New Jersey, 1995.
2. L. Dhar, A. Hale, H.E. Katz, M.L. Schilling, M.G. Schnoes, and F.C. Schilling, Recording media that exhibit high dynamic range for digital holographic data storage, Opt. Lett., 24, pp. 487–489 (1999).
3. W.L. Wilson, K. Curtis, M. Tackitt, A. Hill, A. Hale, M. Schilling, C. Boyd, S. Campbell, L. Dhar, and A. Harris, High density, high performance optical data storage via volume holography: Viability at last? Optical and Quantum Electronics, 32, pp. 393–404 (2000).
4. R.T. Ingwall and D. Waldman, Photopolymer systems, in H.J. Coufal, D. Psaltis, and G.T. Sincerbox, Eds., Holographic Data Storage, Springer-Verlag, New York, 2000, pp. 171–197.
5. L. Dhar, M.G. Schnoes, H.E. Katz, A. Hale, M.L. Schilling, and A.L. Harris, Photopolymers for digital holographic data storage, in H.J. Coufal, D. Psaltis, and G.T. Sincerbox, Eds., Holographic Data Storage, Springer-Verlag, New York, 2000, pp. 200–208.
6. T. Bieringer, Photoaddressable polymers, in H.J. Coufal, D. Psaltis, and G.T. Sincerbox, Eds., Holographic Data Storage, Springer-Verlag, New York, 2000, pp. 209–228.
7. C.C. Bowley and G.P. Crawford, Diffusion kinetics of formation of holographic polymer-dispersed liquid crystal display materials, Appl. Phy. Lett., 76, p. 2235 (2000).
8. K.O. Hill, Y. Fujii, D.C. Johnson, and B.S. Kawasaki, Photosensitivity in optical waveguides: Application to reflection filter fabrication, Appl. Phys. Lett., 32, p. 647 (1978).
9. G. Meltz, W.W. Morey, and W.H. Glenn, Formation of Bragg gratings in optical fibers by transverse holographic method, Opt. Lett., 14, p. 823 (1989).
10. A. Othonos and K. Kalli, Fiber Bragg Gratings: Fundamentals and Applications in Telecommunications and Sensing, Artech House, Boston, 1999.
11. R. Kashyap, Fiber Bragg Gratings, Academic Press, San Diego, 1999.
12. M. Yang and C. Gu, Flattopped tunable wavelength-division-multiplexer filter design, Appl. Opt., 38, pp. 1692–1699 (1999).
13. R.L. Sutherland, L.V. Natarajan, V.P. Tondiglia, T.J. Bunning, and W.W. Adams, Switchable volume hologram material and devices, U.S. Patent #5,942,157, 1996.
14. M. Date, Y. Takeuchi, and K. Kato, Droplet size effect on the memory-mode operating temperature of smectic-A holographic polymer dispersed liquid crystal, Journal of Physics, D-Applied Physics., 32(24), pp. 3164–3168 (1999).
15. K. Tanaka, K. Kato, and M. Date, Fabrication of holographic polymer dispersed liquid crystal (H-PDLC) with high reflection efficiency, Japanese Journal of Applied Physics Part 2-Letters, 38(3A), pp. L277–L278 (1999).
16. T.J. Bunning, L.V. Natarajan, V.P. Tondiglia, and R.L. Sutherland, Holographic polymer-dispersed liquid crystals (H-PDLCs), Annual Review of Materials Science, 30, pp. 83–115 (2000).
17. K. Mimura and K. Sumiyoshi, Diffraction efficiency improvement in Holographic Polymer Dispersed Liquid Crystal (H-PDLC) devices, Molecular Crystals & Liquid Crystals, 346, pp. 239–244 (2000).
18. R.L. Sutherland, Polarization and switching properties of holographic polymer-dispersed liquid-crystal gratings. I. Theoretical model, Journal of the Optical Society of America, B-Optical Physics, 19(12) pp. 2995–3003 (2002).

19. J. Qi, H.Q. Xianyu, J.H. Liang, and G.P. Crawford, Active U-turn electrooptic switch formed in patterned holographic polymer-dispersed liquid crystals, IEEE Photonics Technology Letters, 15(5), pp. 685–687 (2003).
20. C.C. Bowley and G.P. Crawford, Diffusion kinetics of formation of holographic polymer-dispersed liquid crystal display materials, Appl. Phy. Lett., 76, p. 2235 (2000).
21. A.W. Snyder and J.D. Love, Optical Waveguide Theory, Chapman and Hall, London, 1983.
22. C. Vassallo, Rigorous theory for modes of optical fibers with cladding limited by a plane, ibid., 1986, 22, p. 944–945.
23. M.S. Dinleyici and D.B. Patterson, Vector modal solution of evanescent coupler, Journal of Lightwave Technology, 15(12), pp. 2316–2324 (1997).
24. M.S. Dinleyici and D.B. Patterson, Calculation of the wavelength filter properties of the fiber-slab waveguide structure using vector mode expansion, Journal of Lightwave Technology, 16(11), pp. 2034–2039 (1998).
25. D. Marcuse, F. Ladouceur, and J.D. Love, Vector modes of D-shaped fibers, Inst. Elec. Eng. Proc. J., 139, (Apr.), pp. 117–126 (1992).
26. D. Marcuse, Investigation of coupling between a fiber and an infinite slab, Journal of Lightwave Technology, 7(1), pp. 122–130 (1989).
27. M. Yang and C. Gu, Flat-topped tunable wavelength-division-multiplexer filter design, Appl. Opt., 38, pp. 1692–1699 (1999).
28. C. Gu, Y. Xu, Y. Liu, J.J. Pan, F. Zhou, and H. He, Applications of new photorefractive materials in fiber optic devices, SPIE Annual Meeting, Seattle, July 7–11, 2002, paper 4803-17.
29. C. Gu, Y. Xu, Y. Liu, J.J. Pan, F. Zhou, and H. He, Applications of Unconventional Photorefractive Materials in Fibre Devices, J. Opt. A: Pure Appl. Opt. 5, pp. S420–S427 (2003).
30. C. Gu, Y. Xu, Y. Liu, J.J. Pan, F. Zhou, and H. He, Applications of photorefractive materials in information storage, Processing and Communication, Optical Materials, 23, pp. 219–227 (2003).
31. C. Gu, Y. Liu, Y. Xu, J.J. Pan, F. Zhou, and H. He, Send a hologram, IEEE Circuits and Devices, 19(6), pp. 17–23 (2003).
32. V. Srikant, Broadband dispersion and dispersion slope compensation in high bit rate and ultra long haul systems, OFC2001, TuH1-1-3, 2001.
33. K. Aikawa, T. Suzuki, K. Himeno, and A. Wada, New dispersion-flattened hybrid optical fiber link composed of medium-dispersion large-effective-area fiber and negative dispersion fiber, OFC 2001, TuH6-1-3, 2001.
34. M. Shirasaki, Compensation of chromatic dispersion and dispersion slope using a virtually imaged phased array, OFC 2001, TuS1-1-3, 2001.
35. M. Ibsen, M.K. Durkin, M.J. Cole, and R.I. Laming, Sinc-sampled fiber Bragg gratings for identical multiple wavelength operation, IEEE Photonics Technology Letters, 10, pp. 842–844 (1998).
36. Y. Xie, S. Lee, Z. Pan, J.X. Cai, A.E. Willner, V. Grubsky, D.S. Starodubov, E. Salik, and J. Feinberg, Tunable compensation of the dispersion slope mismatch in dispersion-managed systems using a sampled nonlinearly chirped FBG, IEEE Photonics Technology Letters, 12, pp. 1417–1419 (2000).
37. W.H. Loh, F.Q. Zhou, and J.J. Pan, Sampled fiber grating based dispersion slope compensator, IEEE Photonics Technology Letters, 11, pp. 1280–1282 (1999).
38. X. Chen, Y. Luo, C. Fan, T. Wu, and S. Xie, Analytical expression of sampled Bragg gratings with chirp in sampling period and its application in dispersion management design in a WDM system, IEEE Photonics Technology Letters, 12, pp. 1013–1015 (2000).
39. X. Chen, X. Li, L. Xia, J. Wang, S. Xie, and Y. Yin, Numerical investigation of a stress-gradient sampled Bragg grating for dispersion compensation applications in wavelength-division multiplexing systems, Optics Communications, 187, pp. 363–367 (2001).
40. M. Ibsen, R. Feced, P. Petropoulos, and M.N. Zervas, 99.9% Reflectivity dispersion-less square-filter fiber Bragg gratings for high speed DWDM networks, OFC, PD21, Baltimore, 2000.
41. M.K. Durkin, R. Feced, C. Ramirez, and M.N. Zervas, Advanced fibre Bragg gratings for high performance dispersion compensation in DWDM systems, OFC, TuH4-1, 2000.
42. M. Ibsen et al., Broadband fibre gratings for pure thord-order dispersion compensation, OFC, Postdeadline paper FA7-1, 2002.
43. P. Petropoulos, M. Ibsen, A.D. Ellis, and D.J. Richardson, Rectangular pulse generation based on pulse reshaping using a superstructured fiber Bragg grating, Journal of Lightwave Technology, 19(5), pp. 746–752 (2001).
44. P.C. Teh, P. Petropoulos, M. Ibsen, and D.J. Richardson, Phase encoding and decoding of short pulses at 10 Gbit/s using superstructured fiber Bragg gratings, Photonics Technology Letters, 13(2), pp. 154–156 (2001).